Cl–1 doped Sb2Se3 polycrystals and films for optoelectric application

Xue Luo, Yunpeng Wang, Donglou Ren, Rui Zhang, Shuo Chen, Michel Cathelinaud, Yang Xu, Xvsheng Qiao, Xianghua Zhang, Xianping Fan

Credit Author Statement

Xue Luo: Wrote articles and performed experiments as well as data processing and analysis

Yunpeng Wang:Test the micromorphology structure and XPS

Donglou Ren:Revised the article

Rui Zhang:Engaged the analysis of absorption spectrum data

Shuo Chen: Revised the article and guided data processing

Michel Cathelinaud:Guided device design and preparation

Yang Xu: Conceived optoelectronic performance experiment and revised article

Xvsheng Qiao: Designed the micro-rod experiment and revised article

Xianghua Zhang: Undertook the analysis of Hall test data

Xianping Fan: Guided the article ideas and revised articles

Graphic abstract

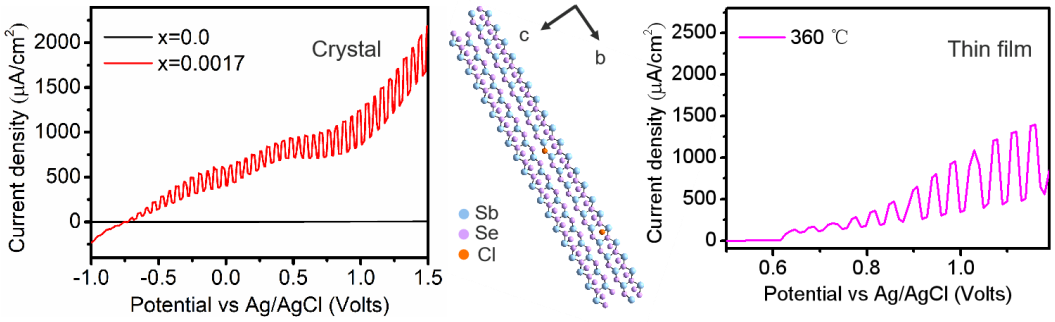

The Cl^--doped $Sb_2(Se_{3-x}Cl_x)_3$ crystals and thin films were prepared using a conventional melt quenching method and thermal evaporation method, respectively. The photoelectric properties of $Sb_2(Se_{3-x}Cl_x)_3$ crystals and thin films have been investigated.

Cl^{-1} doped Sb_2Se_3 Polycrystals and Films for Optoelectric Application

Xue Luo,[a] Yunpeng Wang,[a] Donglou Ren,[b] Rui Zhang,[a] Shuo Chen,[c] Michel Cathelinaud,[b] Yang Xu,[d] Xvsheng Qiao,[a,*] Xianghua Zhang,[b,*] and Xianping Fan[a,*]

[a] *State Key Laboratory of Silicon Materials & School of Materials Science and Engineering, Zhejiang University, Hangzhou, 310027, P. R. China.*

[b] *Laboratory of Glasses and Ceramics, Institute of Chemistry, CNRS-Université de Rennes I, Campus de Beaulieu, 35042 Rennes cedex, France*

[c] *Shenzhen Key Laboratory of Advanced Thin Films and Applications, College of Physics and Optoelectronic Engineering, Shenzhen University, Shenzhen, 518060, P. R. China.*

[d] *College of Materials and Chemistry, China Jiliang University, Hangzhou 310018, China.*

[e] *Ocean Academy, Zhejiang University, Zhoushan 316021, China.*

Abstract

Antimony selenide (Sb_2Se_3) has been considered potential candidate material for the high-performance photovoltaic and photo-detecting application due to its significant optical absorption coefficient (~10^5), suitable direct band gap (1.0 ~ 1.2 eV), low toxicity, and natural abundance in the crust. To overcome its low electrical conductivity and low-charge carrier density deficiencies, we propose a one-step melting quenching method strategy to prepare Cl^- doped Sb_2Se_3 semiconductors. The photocurrent density

of $Sb_2(Se_{0.9983}Cl_{0.0017})_3$ crystal was greatly improved, with fast response speed and photo-response stability. The $Sb_2(Se_{0.9983}Cl_{0.0017})_3$ films were then fabricated with rapid thermal evaporation. The beneficial effect of $Sb_2(Se_{0.9983}Cl_{0.0017})_3$ films on photoelectric performance enhancement is confirmed by researching aspects such as heat treatment-dependent morphology, growth orientation and photoconductivity.

Key words: Sb_2Se_3, doping, n-type, optoelectronic application, DFT calculations

Introduction

Sb_2Se_3 has been widely used in many fields, including high-performance photodetectors, solar cells, thermoelectric devices, as well as for other important applications.[1-5] As a thin-film photovoltaic material, Sb_2Se_3 has many advantages, such as a high absorption coefficient, a direct band gap of 1.18 eV, non-toxic chemistry, a simple binary material nature, and low grain boundary complexation.[6-8] Despite the many advantages of Sb_2Se_3 as an absorber material, the application time of Sb_2Se_3-mediated meterials is relatively short in photovoltaics before 2009. Recently, Messina et al. have proposed that they achieved a power conversion efficiency (PCE) of 0.66% using a solution deposition process.[9] However, *the field has overgrown in the recent years, achieving maximum efficiency of 9.2% for Sb_2Se_3-based photovoltaic devices in 2019*.[10] This rapid growth in efficiency implies Sb_2Se_3 with a vast application potential . In most current studies, Sb_2Se_3 is considered as a p-type semiconductor, and there are fewer reports on n-type Sb_2Se_3. In addition, the inherent low conductivity of

Sb_2Se_3 (10^{-6} $\Omega^{-1}\cdot m^{-1}$) limits its application in high-performance optoelectronic devices, and doping is an effective way to improve the conductivity of the material. By *employing doping to* introduce Cl^{-1} ions*, n-type semiconductors can be obtained, and the low conductivity and low carrier concentration can be effectively improved*.

In this work, we prepared Cl^--doped $Sb_2(Se_{1-x}Cl_x)_3$ crystals using a conventional melt quenching method with vacuum-sealed quartz tubes, and it was shown that $Sb_2(Se_{1-x}Cl_x)_3$ is an n-type semiconductor. The effects of Cl^- doping on the structure, morphology and photoelectric properties of Sb_2Se_3 were investigated, and the electrical and photoelectric conductivities of Sb_2Se_3 were significantly increased after doping. On this basis, Cl^- doped Sb_2Se_3 monolayer films were prepared by a thermal evaporation method using $Sb_2(Se_{1-x}Cl_x)_3$ crystals as the target material, and the effects of different heat treatment temperatures on the film morphology and photoconductivity properties were analysed.

Experiments

Materials

Sb shot (Alfa Aesar, 99.999%, 6 mm,), Se shot (Alfa Aesar, 99.999%) and $SbCl_3$ (Alfa Aesar, 99.9%).

Synthesis of $Sb_2(Se_{3-x}Cl_x)_3$ Crystals

First, the raw materials were weighed according to the different chemical compositions according to formula $Sb_2(Se_{1-x}Cl_x)_3$ (where x = 0, 0.0008, 0.0017, 0.0025 and 0.0033; 6g mixture for each sample, and corresponding mole ratios of Cl are 0,

0.25%, 0.5%, 0.75% and 1%), and then loaded into a thoroughly cleaned silica tube (with an inner diameter of 10mm and an outer diameter of 14 mm). The tube was then evacuated to a vacuum of around 10^{-5} mbar and sealed. The sealed tube was heated to 750 °C at a 1.15 ℃/min rate in a rocking furnace. Then, it was held at this temperature for eight hours. Subsequently, the tube was taken out and quenched in water at room temperature. Finally, the bulks were annealed at 350 °C for three hours to reduce the mechanical stress generated in the quenching process. It was cut and polished into discs with 2 mm thickness for subsequent characterization.

Fabrication of $Sb_2(Se_{0.9983}Cl_{0.0017})_3$Thin Film

The $Sb_2(Se_{0.9983}Cl_{0.0017})_3$ sample was used as the evaporation source, and the evaporation vessel was a graphite crucible. The substrates were commercial FTO (2.5 cm×2.5 cm), ultrasonically cleaned with detergent, acetone, ethanol, and deionized water for 30 minutes before the deposition. Afterwards, the cleaned substrates were blown with dry nitrogen, fixed in the mould and placed on a rotary evaporation plate. After placing the crucible and the substrate, close the hatch, evacuate to below 10-6m bar, turn on the evaporation power supply, control the evaporation speed at two nm/s by adjusting the current and control the film thickness by controlling the deposition time. All film thicknesses were controlled around 350 nm. After evaporation, turn off the evaporation power and vacuum pump and take out the sample. Finally, the samples were heat-treated in a tube furnace, vented with argon, and heat-treated at different temperatures for 15 min.

Characterization

The crystal structure of as-prepared samples was obtained by X-ray diffraction (XRD) using a Bruker AXS D8 Advance X-ray diffractometer (Karlsruhe, Germany) with Cu-Kα radiation at a scan rate of 0.02° s^{-1}. The morphology and composition were observed by a JEOL JSM-7100 F thermal field emission electron microscopy equipped with energy-dispersive X-ray spectroscopy (EDXS) operating at 20 kV. Transmission electron microscopy (TEM) and corresponding selected area electron diffraction (SAED) were examined by an FEI Tecnai G2F20 field-emission transmission electron microscope operating at an acceleration voltage of 200 kV. The actual concentration of Cl was determined with the Eschka method [11].The electrical properties were measured by a Hall test (Bio-Rad HL5500PC) at room temperature. A slide wafer was cut from the as-synthesized bulk sample, and the gold contacts were deposited using thermal evaporation. The optical properties were measured using a UV–vis spectrometer (SHIMADZU UV-3150). The element composition was analysed using X-ray photoelectron spectroscopy (XPS, ESCALAB). The photoelectric performance was evaluated by photo-electro-chemical (PEC) measurements using the typical 3-electrode method where Ag/AgCl, Pt-wire, and our bulk samples were treated as the reference electrode counter electrode and the working electrode, respectively.

Moreover, to fabricate the working electrode, well-polished samples with a diameter of 10 mm and a thickness of about 2 mm were homogeneously painted with silver paste on the surface and connected with a copper wire as the back contact.

Afterwards, the back contact was covered with a layer of epoxy resin to avoid a short circuit. A 0.5M LiClO4 solution was used as an electrolyte, and a white light tungsten halogen lamp was applied as the light source. The current-voltage characteristics were recorded with an Autolab Metrohm potentiostat, and a mechanical chopper made the chopped light. All the calculations are performed within the density functional theory (DFT) as implemented in the Vienna Ab initio Simulation Package (VASP) code.

Results and Discussions

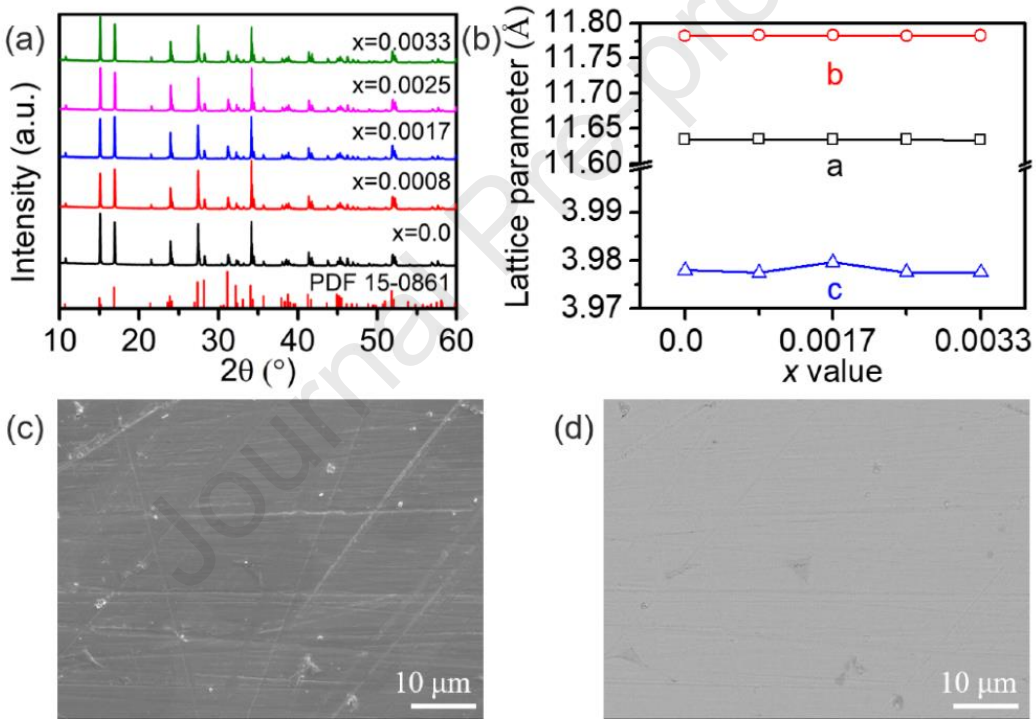

Figure 1 (a) XRD patterns of the bulk $Sb_2(Se_{1-x}Cl_x)_3$ crystals x=0.00,0.0008,0.0017,0.0025 and 0.0033), (b) Lattice constants a, b and c plotted as a function of Cl^- doping concentration, (c) SEM image of the $Sb_2(Se_{0.9983}Cl_{0.0017})_3$ crystal, (d) backscattered electron image of the $Sb_2(Se_{0.9983}Cl_{0.0017})_3$ crystal.

The XRD patterns of Sb_2Se_3 crystals with different Cl^- doping concentrations and pure Sb_2Se_3 crystals are shown in **Figure** 1a. All samples are well matched with the Sb_2Se_3 crystalline phase with standard JCPDS card No. 15-0861, which is an orthorhombic phase with *Pbnm* space group[12]. No other crystalline XRD peaks are

observed in the samples. It indicats that there are neither second phases nor oriented growth for any of the Cl^- doped samples. **Figure** 1b shows the lattice constants a, b, and c obtained for different doping concentrations by Rietveld refinement using the FULL-PROF program. It could be seen that a and b do not change significantly with increasing doping content. The lattice constant c tends to decrease and then grow with the increase of Cl- content, which is consistent with the trend of cell volume change (**Figure** S1). The radius of Cl^- is 0.181 nm is smaller than that of Se^{2-}(0.198 nm)[13], matching the theoretical criterion for solid substitution solution proposed by Hume-Rothery that the difference in radii between the solid solution atom and the substituted atom should be less than 15%. Therefore, with the increasing of Cl^- doping concentration, the lattice constant will become smaller in theoretically. However, the effect of Cl substitution on lattice expansion/shrinking is redundant, which can be contributed to the following reasons. The mole ratio of Cl in the raw materials is small, meanwhile the radius of Cl^- is similar with that of Se^{2-}. Besides, when the chloride ion replaces the selenium ion, the gravitational force between Cl^- and Sb^{3+} becomes weaker because the charge of Cl^- is lower than that of Se^{2-}, and the doping of Cl^- with a smaller radius will cause the lattice expansion instead[14]. So the c lattice parameter and cell volume is fluctuating.

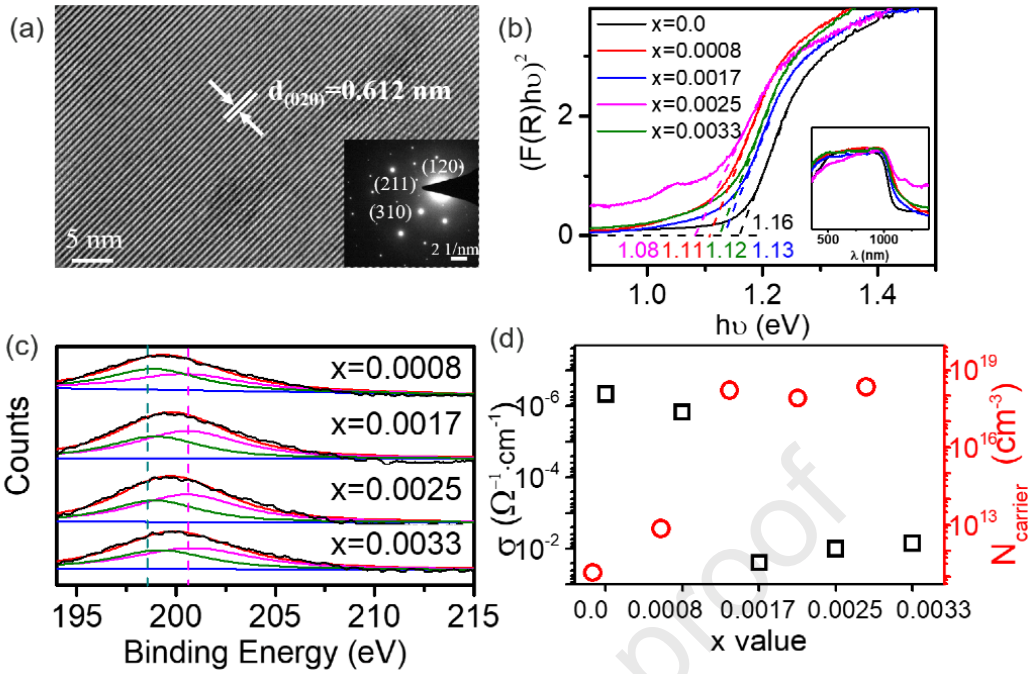

Figure 2 (a) HRTEM image of the $Sb_2(Se_{0.9983}Cl_{0.0017})_3$ crystal (the insets are the electron diffraction patterns by fast Fourier transforming of the selected area corresponding to (a), where the scale bars stand for 2 1/nm), (b) A plot of $[F(R)h\upsilon]^2$ vs. energy for different Cl concentration samples (the inset is the corresponding optical absorption spectra), (c) XPS spectra of the samples with different Cl^- concentrations, (d) electrical resistivity and carrier concentration plotted as a function of Cl^- doping concentration (x value).

Here, we take the polished $Sb_2(Se_{0.9983}Cl_{0.0017})_3$ sample as an example (the SEM images and backscattered electron images of other samples can be found in **Figure** S2 and **Figure** S3, respectively); the SEM image and corresponding backscattered electron image of the $Sb_2(Se_{0.9983}Cl_{0.0017})_3$ sample is shown in **Figure**s1c and 1d, respectively. The surface of $Sb_2(Se_{0.9983}Cl_{0.0017})_3$ is smooth and crack-free, and the surface scratches are polishing traces. The backscattering analysis can be used to analyse the bulk samples' weave organisation, elemental enrichment, etc. From the backscattered images, there are neither second phases nor elemental enrichment in all the samples, in agreement with the XRD results. The EDXS elemental mapping (see **Figure** S4) shows the elemental distribution, where Sb, Se, and Cl elements are uniformly distributed in

all the samples. Although all the Cl concentration, except x = 0.0033, are under the detection limit of the EDXS measurements, the molar ratio of Sb/Se could be obtained from the EDXS results, as listed in Table S1. In order to further quantitively determine the actual concentration of Cl, we further tested the samples to determine the Cl concentration according to the Eschka method [11]. In results, the Cl concentrations were determined as 0.015 wt %, 0.110 wt %, 0.128 wt % and 0.599 wt, as list in Table S2. Then, the actual formula of, as list in Table S3, were determined as $Sb_2Se_{3.133}Cl_{0.002}$, $Sb_2Se_{3.056}Cl_{0.015}$, $Sb_2Se_{3.187}Cl_{0.018}$ and $Sb_2Se_{3.153}Cl_{0.084}$, as x = 0.0008, 0.0017, 0.0025 and 0.0033, respectively. To keep the consistence of the context, we still name all the sample with the norminal $Sb_2Se_{3(1-x)}Cl_{3x}$ sample names, such as $Sb_2(Se_{0.9983}Cl_{0.0017})_3$.

Figure 2a shows a high-resolution transmission electron microscopy photo of $Sb_2(Se_{0.9983}Cl_{0.0017})_3$, where clear lattice stripes can be observed, indicating the excellent crystallinity of the sample. The lattice spacing revealed in the HRTEM image is 0.612 nm, corresponding to the [020] crystal plane of the orthorhombic Sb_2Se_3 phase. The inset of the HRTEM image is the corresponding selected electron diffraction pattern, which shows a series of diffraction rings. Such a characteristic diffraction pattern of ~~a~~ the crystalline phase region reflects the high crystallinity of the sample. The three diffractions are attributed to the [120], [311], and [310] crystallographic plane.

The optical reflectance spectra of pure Sb_2Se_3 and $Sb_2(Se_{1-x}Cl_x)_3$ crystals are shown in **Figure** 2b. The reflectance R ~~obtained from the test~~ can be converted by $F(R)=(1-R)^2/(2R)$ to obtain the inset absorption spectra. All samples have strong absorption

in the visible to the near-infrared range, and the doped samples have a slight red-shift in the absorption range compared with pure Sb_2Se_3, which broadens the spectral response range of the samples. Since Sb_2Se_3 has a direct band gap, according to the Tauc formula, we plotted the energy *hv* as the horizontal coordinate and $[F(R)hv]^2$ as the vertical coordinate to obtain the band gap (forbidden bandwidth) value of the material after linear extrapolation. The **Figure** shows that the band gap value of pure Sb_2Se_3 is 1.16 eV, and all samples' band gaps produced a different degree of reduction after doping. This result may be due to the synergistic effect of Burstein-Moss displacements and reformation effects [15, 16]. **Figure** 2c shows the XPS spectra of the bulk samples at different Cl- doping concentrations, and after fitting all samples, there are two peaks around the 198.7 eV and 200.6 eV positions, which correspond to the Cl^- 2p1/2 and Cl^- 2p3/2 characteristic peaks of Cl^-, respectively[17]. Furthermore, with the change in doping concentration, the position of the peaks does not change much, and the intensity does not change significantly. The XPS spectra of Sb-3d and Se-3d are shown in the **Figure** S5.

Hall tests were performed at room temperature to evaluate the various electrical properties of the samples. The carrier concentration and resistivity data for pure Sb_2Se_3 crystals and $Sb_2(Se_{3-x}Cl_x)_3$ crystals are shown in **Figure** 2d. It can be seen that the resistivity of pure Sb_2Se_3 crystals is very high, about 2×10^6 Ω·cm. When x is equal to 0.0017, the resistivity of the samples is improved somewhat, decreasing to 10^5 orders of magnitude. When the doping concentration was further increased, the resistivity of

the samples was significantly reduced to 10^2, which is four orders of magnitude lower than in pure Sb_2Se_3. Meanwhile, the electrical conductivity was found to be significantly improved after doping. In addition, the carrier concentration also shows a similar trend to the resistivity properties before and after doping. At lower doping concentrations, the x=0.0017 sample (7.144×10^{12} cm^{-3}) has a *slight* increase in carrier concentration relative to the Sb_2Se_3 crystal (1.44×10^{11} cm^{-3}), and the carrier concentration reaches the order of 10^{18} cm^{-3} after the doping concentration continues to increase.

The increased carrier concentration can be attributed to Cl^- doping. The functional relation between the defect formation energy and Fermi level of Cl^- induced defects in Se-poor and Se-rich conditions and the defect transition energy level of Cl^- doped defects are calculated, and the results are shown in **Figure** 3. Cl_{Se} is the desired sender defect for forming p-type semiconductors, and calculations show that the primary newly introduced defects in $Sb_2(Se_{1-x}Cl_x)_3$ because Cl doping are Cl_{Se}, Cl_i and Cl_{Sb}. The defect formation energy of Cl_{Se} is 0.05 eV at CBM 0.05 eV, Cl_{Se} is a shallow energy level sender defect with low defect formation energy, and, thus it becomes the primary source of electron carrier formation. Cl_i and Cl_{Sb} are both deep energy level host defects, which will produce harmful defect complex centers in the whole system; however, they both have higher formation energy, 1.9 eV for Cl_i and 1.7 eV for Cl_{Sb} under rich selenium conditions, so these two defects are not easy to form. So Cl_{Se} is the *primary* defect type after Cl doping, and Cl replaces Se^{2-} in Sb_2Se_3 with an extra electron, which

can be written as:

$$Cl_{Se}^{\times} \rightarrow Cl_{Se}^{\cdot} + e' \quad (1)$$

Whereas, the electron is weakly bound to the $Cl_{Se}^{\cdot}$ the energy lower than the bandgap of Sb_2Se_3 is required to allow this electron to become a drifting carrier in the crystal[18]. Due to the increase in electron carriers, the carrier concentration in $Sb_2(Se_{1-x}Cl_x)_3$ crystal is increased substantially. The equation (2) can express the relationship between the resistivity and the carrier concentration of materials:[18]

$$1/\rho = ne\mu \quad (2)$$

where ρ is the resistivity, n is the charge carrier concentration, e is the amount of charge per unit, and μ is the mobility. Therefore, when the carrier concentration is substantially increased after Cl doping, the high resistivity of Sb_2Se_3 crystals is observed to be reduced by about four orders of magnitude. In addition, Cl doping leads to an upward shift of the valence band and a reduction of the band gap of $Sb_2(Se_{1-x}Cl_x)_3$ crystals due to the Coulomb interaction between Cl ions and holes. This phenomenon is also reflected in the UV-Vis diffuse reflectance spectra, where the reduction of the band gap leads to a red shift of the absorption band. Those permit $Sb_2(Se_{1-x}Cl_x)_3$ crystals to be an optically active materials in the near-infrared spectral region. More importantly, both resistivity and carrier concentration are also significantly improved after doping, and these performance enhancements are ultimately beneficial to obtain high-performance optoelectronic and photovoltaic devices, thus further confirming the successful doping of Cl ions.

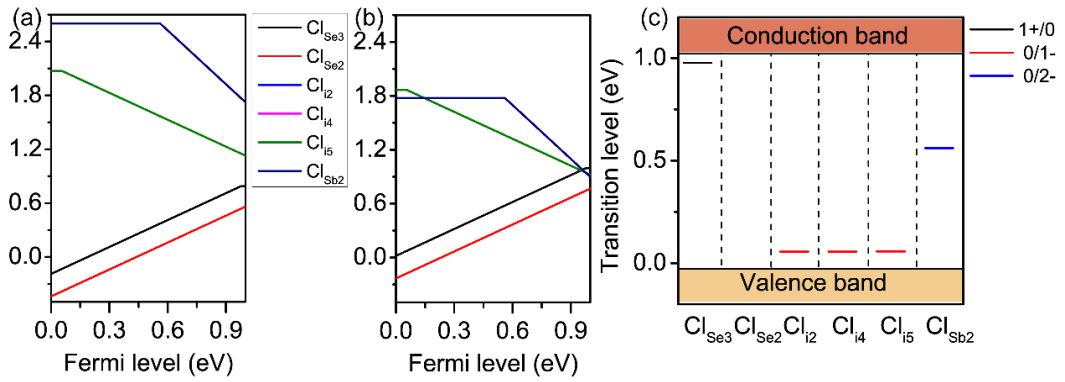

Figure 3 Cl^- doped Sb_2Se_3 defect formation energy as a function of Fermi level under (a) Se-deficient and (b) Se-rich conditions. (c) Defect transition level diagram.

The conduction type and mobility of $Sb_2(Se_{1-x}Cl_x)_3$ crystals are listed in Table.1, where the undoped Sb_2Se_3 crystals exhibit intrinsic p-type conductivity, and the Cl^- doped samples eventually exhibit n-type conductivity. The samples eventually exhibit n-type conductivity because Cl^- replaces Se^{2-} in Sb_2Se_3 and thus brings an extra electron, so that the Cl^- doped bulk $Sb_2(Se_{1-x}Cl_x)_3$ crystals eventually behaves as an n-type semiconductor [19]. The presence of Cl^- is also demonstrated in the XPS results. Besides the conductivity type changing, the increase of electron carriers also raises the carrier concentration of the material, where the results are shown in **Figure** 2d. The mobility of the carriers is up to 7.63 $cm^2/v{\cdot}s$ at $x = 0.0025$ after doping, which is nearly 16 times higher than that of pure Sb_2Se_3 crystals (0.481 $cm^2/v{\cdot}s$). All these results indicate that the electrical properties of the crystals are improved after Cl^- doping, and it is favorite to various photoelectric applications.

Table 1 Electrical properties of the $Sb_2(Se_{1-x}Cl_x)_3$ polycrystals.

	x=0.0	x=0.0008	x=0.0017	x=0.0025	x=0.0033
Conduction type	p	n	n	n	n
Mobility ($cm^2/v{\cdot}s$)	0.481	1.31	0.951	7.63	2.03

The photoconductivity of $Sb_2(Se_{1-x}Cl_x)_3$ crystals are tested using a three-electrode photoelectrochemical (PEC) system [20], where the schematic diagram of the three-electrode system and the physical diagram of the working electrode are shown in **Figure** 4a and 4b. The light source intensity for the test was 22.51 mW/cm^2, and Sb_2Se_3 crystals with different Cl^- doping contents are tested as the working electrode. When the Cl^- doping content is low (x=0.0008), its photocurrent density at -1.5V bias voltage is as small as about 55 μA/cm^2. The improved photocurrent density, compared with pure Sb_2Se_3, can be observed from **Figure** 4c. And with the increase of doping content, the photocurrent density of the $Sb_2(Se_{0.9983}Cl_{0.0017})_3$ sample obtained a significant improvement of about 360 μA/cm^2, which is about 360 times than that of pure Sb_2Se_3. This excellent performance also corresponds to the more considerable carrier mobility and carrier concentration in the previous section, the free electrons introduced in Sb_2Se_3 after Cl doping enable $Sb_2(Se_{1-x}Cl_x)_3$ crystals to generate more photogenerated carriers under the same light irradiation compared to pure Sb_2Se_3 crystals. The enhanced conductivity and mobility allow the photogenerated carriers to be better transported from the inside of the materials to the external circuit, avoiding the compounding of electron-hole pairs, thus allowing a significant increase in photocurrent. It evidences that the Cl doping can substantially improve the photoelectric response of the $Sb_2(Se_{1-x}Cl_x)_3$ polycrystals. Nevertheless, when the doping concentration is varying from x = 0.0025 to 0.0033, the photocurrent density decreases significantly, maybe becasue the excess introduction of Cl brings high defect concentration, and ultimately give a negtive

influece on the photoelectric performance of the samples.[21] In addition, the photocurrents of all the samples have a negative bias, so we can conclude that the Cl^- doped Sb_2Se_3 crystals are n-type semiconductors. This result is also consistent with the previous Hall test results. **Figure** 4d shows the photocurrent densities of pure Sb_2Se_3 and $Sb_2(Se_{0.9983}Cl_{0.0017})_3$ samples, where it is more clearly and intuitively that the photocurrents of the doped samples are greatly enhanced. At the same time, the low photocurrent density of pure Sb_2Se_3 crystal samples also corresponds to its inherent low conductivity and carrier density.

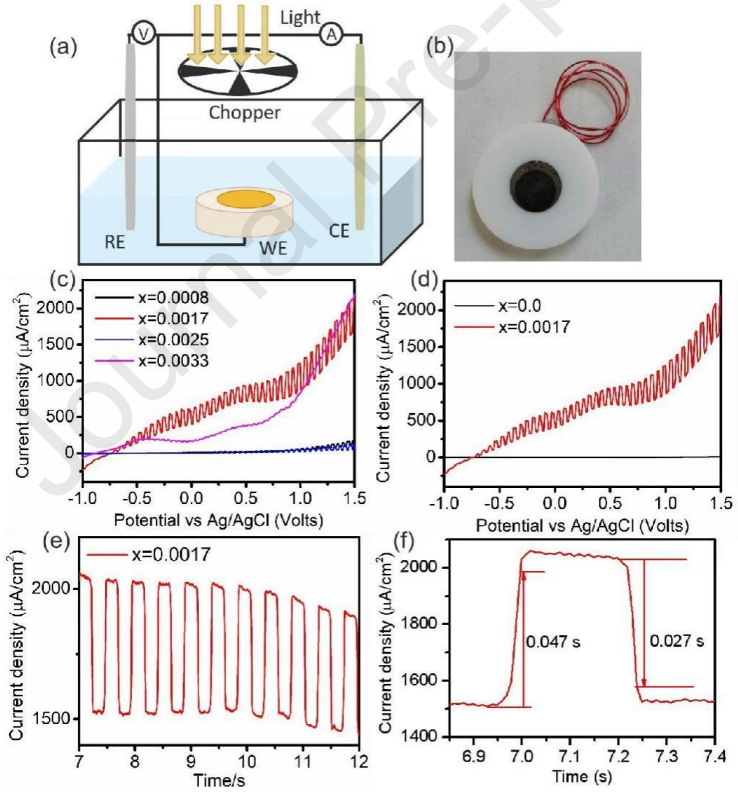

Figure 4 (a) schematic illustration of the 3-electrode photo-electro-chemical (PEC) measurement (b); and image of the fabricated working electrode, (c) Current-voltage characteristics of doped Sb_2Se_3 crystals as working electrodes with different Cl^- doping concentrations, (d) Current-voltage characteristics of pure Sb_2Se_3 crystal and $Sb_2(Se_{0.9983}Cl_{0.0017})_3$ crystal,(e) magnified plot of response cycle in $Sb_2(Se_{0.9983}Cl_{0.0017})_3$ and (f) response and recovery time of $Sb_2(Se_{0.9983}Cl_{0.0017})_3$.

Besides the photocurrent density, the photocurrent stability and the response speed

are of importance to evaluate the device's performance. **Figure** 4e shows the cyclic photoresponse results of the $Sb_2(Se_{0.9983}Cl_{0.0017})_3$ sample, where the photocurrent does not change significantly after nearly ten cycles. This finding indicates that the doped sample has excellent repeatability and stability performance. To calculate the response and recovery rate of the sample, we scaled up one response cycle, as shown in Fig.4f. The response and recovery times of the sample are 0.047 s and 0.027 s, respectively. It thus shows the photoresponse with the quick response and recovery. This result is similar to those reported for some high-performance photodetectors[21, 22], demonstrating the potential of Cl^- doped Sb_2Se_3 crystals for high-performance photodetector applications.

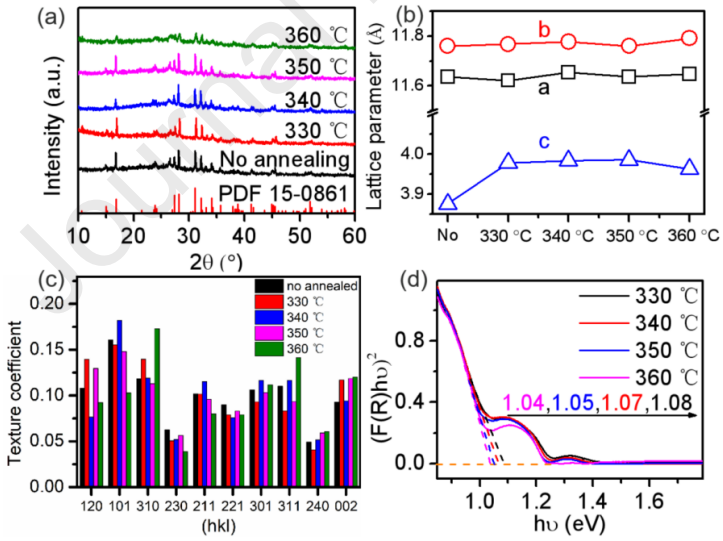

Figure 5 (a) XRD patterns of the $Sb_2(Se_{0.99833}Cl_{0.00167})_3$ films under different annealed temperatures. (b) Lattice constants a, b and c plotted as a function of annealed temperature, (c) texture coefficients of XRD diffraction peaks based on $Sb_2(Se_{0.9983}Cl_{0.0017})_3$ films under different annealing temperatures, (d) A plot of $[F(R)h\upsilon]^2$ vs. energy.

The $Sb_2(Se_{0.9983}Cl_{0.0017})_3$ thin films were prepared with the rapid thermal evaporation method by using $Sb_2(Se_{0.9983}Cl_{0.0017})_3$ crystals as the evaporation source. The XRD patterns of the $Sb_2(Se_{0.9983}Cl_{0.0017})_3$ thin film samples heat-treated at different

temperatures for 15 min are shown in **Figure** 5a. No impurity peaks were detected in all the samples, which proved that no second phase was generated. All samples could correspond to the orthorhombic Sb_2Se_3 crystalline phase (Standard JCPDS Card No. 15-0861). The film samples without heat treatment also have sharp diffraction peaks, indicating that the films prepared by rapid thermal evaporation have crystallised and have good crystallisation properties. The intensity of the diffraction peaks did not change significantly with the heat treatment temperature below 350 °C. When the heat treatment temperature was increased to 360 °C, the intensity of the diffraction peaks greatly decreased, and the width of the diffraction peaks increased. That is because the very high vapour pressure of Sb_2Se_3 at 360 °C results in the poor quality of the films[23]. Similarly, the lattice constants of the film samples were obtained after Rietveld refinement using the FULL-PROF program, as displayed in **Figure** 5b. No significant changes are found for the lattice parameters a and b at different heat treatment temperatures. In contrast, the lattice constant c increased more considerably after the heat treatment, probably due to the redistribution of Cl^- on the surface and in the body with the increase of the heat treatment temperature leading to the lattice expansion[24].

In order to quantify the crystal orientation of the film, we characterize the orientation by the texture coefficient of the diffraction peak, which is calculated as follows [25]:

$$TC_{hkl} = \frac{I_{(hkl)}}{I_{0(hkl)}} \left(\frac{1}{N} \sum_N \frac{I_{(hkl)}}{I_{0(hkl)}}\right) \quad (3)$$

where $I_{(hkl)}$ is the measured diffraction peak intensity of the (hkl) crystal plane, $I_{0(hkl)}$ is

the diffraction peak intensity of the (hkl) crystal plane in Standard JCPDS Card 15-0861, and N is the total number of crystal planes. Large texture coefficients imply a selective orientation growth in the film [26, 27]. **Figure** 4c shows the texture coefficients of some crystalline planes at different heat treatment temperatures, where the (101) and (310) crystalline planes have higher TC values. Due to the unique structure of antimony selenide, the (hk1) orientation ("1" stands for one) is more favorable for device efficiency, while the sample heat-treated at 340 °C has the strongest (hk1) orientation texture coefficient among all. With the heat treatment temperature increases to 360 °C, the texture coefficient of (310) crystal planes (other than (hk1)) rises substantially, which is not favorable to the transportion of photogenerated carriers.

The diffuse reflectance of the films at different heat treatment temperatures was tested using UV-Vis diffuse reflectance spectroscopy, and the absorption spectra (400-1500 nm) and the forbidden bandwidths in **Figure** 5d were obtained by conversion of the equations. The films have strong absorption from the visible range to the near-infrared range, with a clear absorption peak of around 1000 nm, which can extend the absorption range of the films and utilise the near-infrared light. After the heat treatment, the forbidden bandwidths of the samples decreased compared with those of pure Sb_2Se_3, which is consistent with the change in the forbidden band of the bulk samples, and the effect of temperature change on the forbidden bandwidths was not significant.

The SEM images, with the related cross-section images, of the $Sb_2(Se_{0.9983}Cl_{0.0017})_3$ films heat treated at different temperatures are shown in **Figure** 6. At the low

temperature, the grain size in the film is about 300 nm, and there are some voids at the grain boundaries and some small grains on the surface. When the temperature is up to 350 °C, the grain size becomes as large as about 1 μm, where all the voids disappear and the film becomes denser. The deposition thickness of the films can be evaluated from the cross-sectional images, where all the films is around 350 nm thick. In addition,

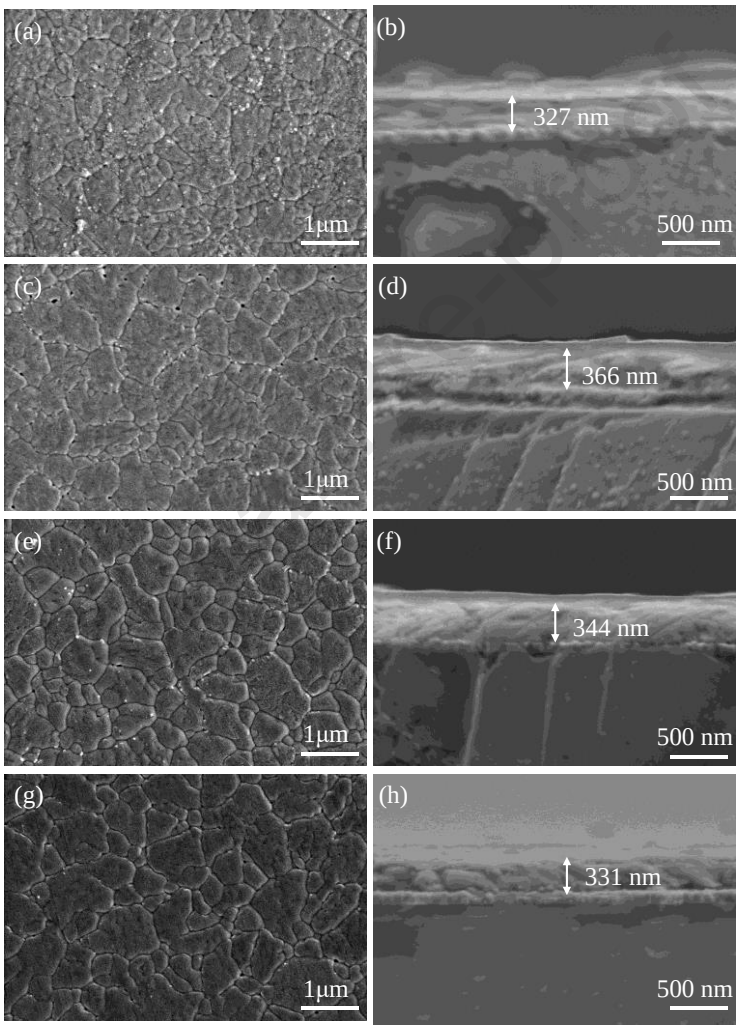

Figure 6 Top views and cross-section SEM images of $Sb_2(Se_{0.9983}Cl_{0.0017})_3$ films on FTO substrates with different annealing temperatures: (a, b) 330 ºC, (c, d) 340 ºC, (e, f) 350 °C and (g, h) 360 ºC.

no defects perpendicular to the substrate were found in cross-sections, indicating that the deposited films were dense. The EDXS of the $Sb_2(Se_{0.9983}Cl_{0.0017})_3$ films heat-treated at 350 °C for 15 min are shown in **Figure** S6. The Sb, Se, and Cl elements are

uniformly distributed in the films without enriched regions. The energy spectra of the samples at different heat treatment temperatures were similarly distributed.

Table 2 Electrical Properties of the Synthesized Cl^- doped films heat treated at different temperatures.

Temperature	Mob($cm^2/V·s$)	Carrier concentration($/cm^3$)	Conductive type
330 °C	26.8	$1.382*10^{20}$	n
340 °C	20.1	$1.772*10^{20}$	n
350 °C	18.8	$2.243*10^{20}$	n
360 °C	100	$3.659*10^{19}$	n

The electrical properties of the film samples at different heat treatment temperatures are obtained from Hall tests at room temperature and are summarized in **Table** 2. All the films exhibit n-type semiconductors at different heat treatment temperatures, consistent with the block conductivity type. The mobility is basically around 20 $cm^2/V·s$ below 350 °C and increases to 100 $cm^2/V·s$ when the heat treatment temperature is increased to 360 °C. This may be due to the higher heat treatment temperature, the more prominent grains, the less grain boundaries, and ultimately increased mobility. The carrier concentration of the films is also higher at around 10^{20}, and these excellent electrical properties indicate that the $Sb_2(Se_{0.9983}Cl_{0.0017})_3$ films have great potential for subsequent applications in photovoltaics.

The photoconductive properties of the films were tested at a light intensity of 7 mW/cm^2 using the films at different heat treatment temperatures as working electrodes. **Figure** 7 shows the photoconductive properties of heat treatment at 340 and 360 °C, while **Figure** S7 shows the photoconductive properties of heat-treated at 330 and 350 °C. The photocurrents of the two samples have a positive bias **(Figure**s 7a-b), indicating that the samples are n-type semiconductors, which is also well agreement

with the Hall test results in the **Table** 2. The photocurrent densities of the films were 956 and 851 μA/cm^2. After heat treatment at 340 °C and 360 °C at a bias voltage of 1.2 V, the films showed the maximum photocurrent density at 340 °C because the films had the maximum (hk1) at this temperature, and this crystal growth direction was favorable for the carrier transport. The photocurrent density is also significant at 360 °C since the films have the most carrier mobility under heat treatment at 360 °C, thus allowing better transport of the generated photoelectrons.

To evaluate the stability of the thin film photoresponse, the cyclic photoresponse performance of the samples are tested and the results are shown in **Figure** 7c and 7d. The photocurrent repetition performance is poor at lower heat treatment temperatures (340 °C), and it gradually decreases with cyclic photocurrent due to some holes on the surface of the films. These defects hinder the compounding and separation of electron-hole pairs. When the temperature increased to 360 °C, the photocurrent did not change significantly even after ten cycles, showing good photocurrent repetition performance. **Figure** 6e and 6f show a magnified view of one response cycle of the thin film sample. At the heat treatment temperature of 360 °C, it has the fastest response and recovery speed of 0.017 s and 0.016 s, respectively. This result is faster than the most rapid response among the bulk materials (0.047 s and 0.027 s), indicating that the Cl^- doped films have the same potential for application in high-performance photodetector devices. The combined photovoltaic performance shows that the films heat-treated at 360 °C have excellent and stable performance. The newly grown $Sb_2(Se_{0.9983}Cl_{0.0017})_3$

crystals are potential candidate materials with application in high-performance photodetectors and photovoltaic devices.

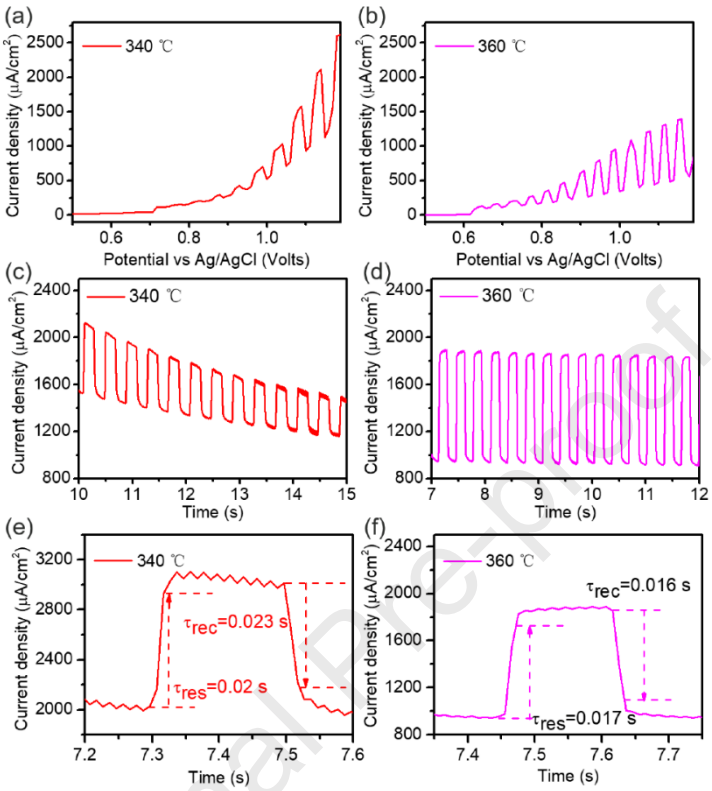

Figure 7 Photoelectrochemical response of post-annealed films on FTO with different annealing temperatures illuminated via a chopped light power density of 7 mW/cm^2: (a) 340 °C, (b) 360 °C; Time-resolved photoresponse of post annealed films on FTO with different annealing temperatures illuminated via a light power density of 7 mW/cm^2: (c) 340 °C, (d) 360 °C; the Magnified plot of one response cycle post annealed films on FTO with different annealing temperatures: (e) 340 °C, (f) 360 °C.

Conclusions

Sb_2Se_3 crystals doped with different degrees of Cl^- content were prepared by the high-temperature melting method. The band gaps of the $Sb_2(Se_{1-x}Cl_x)_3$ crystals were around 1.10 eV and matched with the solar spectrum. Compared with the pure Sb_2Se_3, the electrical properties of the $Sb_2(Se_{1-x}Cl_x)_3$ crystals were substantially improved according to the Hall tests, and the electrical conductivity of $Sb_2(Se_{1-x}Cl_x)_3$ crystals

showed the increment orders of magnitude and reached the minimum at x = 0.0017. Furthermore, the carrier concentration showed a similar trend with Cl^-. With Cl^- doping, the $Sb_2(Se_{1-x}Cl_x)_3$ crystals shifted from p-type to n-type semiconductors. The PEC results showed that the $Sb_2(Se_{0.9983}Cl_{0.0017})_3$ crystal manifested its maximum photocurrent density as about 360 μA/cm^2), which was about 360 times higher than the pure Sb_2Se_3 crystal. Furthermore, the $Sb_2(Se_{0.9983}Cl_{0.0017})_3$ crystal exhibited short responses (0.047 s) and recovery time (0.027 s), as well as a stable photoresponse. The $Sb_2(Se_{0.9983}Cl_{0.0017})_3$ thin films were fabricated through the rapid thermal evaporation method. The subsequent heat treatment at 360 °C was evidenced as the optimal heat treatment temperature to get the preferred (hk1) texture coefficient, the films 'surface with significantly reduced defects, the larger crystal grains, as well as the improved photocurrent density (851 μA/cm^2) and the better repetitive photocurrent stability along with the fast response and recovery time. Therefore, the $Sb_2(Se_{0.9983}Cl_{0.0017})_3$ thin films can be applied to develop high-performance thin-film optoelectronic devices.

AUTHOR INFORMATION

Corresponding Author

* E-mails: X. Qiao (qiaoxus@zju.edu.cn); X. Fan (fanxp@zju.edu.cn); Tel.: +86-571-87951234; X. Zhang (xiang-hua.zhang@univ-rennes1.fr).

ACKNOWLEDGMENT

The authors gratefully acknowledge the financial support from The National Natural Science Foundation of China (No.51802299) and the Open Foundation of Key Laboratory of Rare Earth Optoelectronic Materials and Devices of Zhejiang Province.

SUPPORTING INFORMATION

Figure S1 Lattice cell volumes of the polycrytal samples; **Figure S2** SEM images of the polycrytal samples; **Figure S3** Back-scattered SEM images of the polycrytal samples; **Table S1** The EDXS results of the polycrytal samples; **Table S2** The Cl concentration determined through the Eschka method.; **Table S3** The actual chemical formula of the polycrytal samples; **Figure S4** The EDXS mappings of the polycrytal samples; **Figure S5** (a) Sb-3d and (b) Se-3d XPS spectra of the polycrytal samples; **Figure S6** The EDXS mappings of the $Sb_2(Se_{0.9983}Cl_{0.0017})_3$ films; **Figure S7** Photoelectrochemical curves of the post-annealed $Sb_2(Se_{0.9983}Cl_{0.0017})_3$ films.

Reference

[1] J. Hu, Y. Shi, Z. Zhang, R. Zhi, S. Yang, B. Zou, Recent progress of infrared photodetectors based on lead chalcogenide colloidal quantum dots, Chinese Physics B 28(2) (2019) 020701.

[2] X. Wang, W. Tian, M. Liao, Y. Bando, D. Golberg, Recent advances in solution-processed inorganic nanofilm photodetectors, Chemical Society Reviews 43(5) (2014) 1400-22.

[3] Z. Zeng, T. Sun, J. Zhu, X. Huang, Z. Yin, G. Lu, Z. Fan, Q. Yan, H.H. Hng, H. Zhang, An effective method for the fabrication of few-layer-thick inorganic nanosheets, Angewandte Chemie 51(36) (2012) 9052-6.

[4] L. Zhai, J.-M. Yu, S. Jia, T. Yang, C. Yang, W. Liu, E. Zhang, B. Zheng, W.-W. Xiong, A crystalline organic hybrid indium antimony sulfide for high performance lithium/sodium storage, Journal of Solid State Chemistry 316 (2022) 123637.

[5] R. Wang, M. Wei, G. Jiang, W. Liu, C. Zhu, Study of the Preperation of SnSe Nanorods with Selenium Dioxide as Source, Chemistry Letters 43(5) (2014) 693-695.

[6] G. Chen, W. Wang, C. Wang, T. Ding, Q. Yang, Controlled Synthesis of Ultrathin Sb2Se3 Nanowires and Application for Flexible Photodetectors, Advanced Science 2(10) (2015) 1500109.

[7] M. Wang, W. Wu, X. Zheng, X. Hou, C. Liu, Q. Hao, H. Liu, Preparation of uniform Sb 2 Se 3 nanorods by hot-injection polyol process and their application in photodetector, Materials Letters 193 (2017) 191-194.

[8] Y. Zhou, L. Wang, S. Chen, S. Qin, X. Liu, J. Chen, D.-J. Xue, M. Luo, Y. Cao, Y. Cheng, E.H. Sargent, J. Tang, Thin-film Sb2Se3 photovoltaics with oriented one-dimensional ribbons and benign grain boundaries, Nature Photonics 9(6) (2015) 409-415.

[9] S. Messina, M.T.S. Nair, P.K. Nair, Antimony Selenide Absorber Thin Films in All-Chemically Deposited Solar Cells, Journal of The Electrochemical Society 156(5) (2009) H327.

[10] Z. Li, X. Liang, G. Li, H. Liu, H. Zhang, J. Guo, J. Chen, K. Shen, X. San, W. Yu, R.E.I. Schropp, Y. Mai, 9.2%-efficient core-shell structured antimony selenide nanorod array solar cells, Nature Communications 10(1) (2019) 125.

[11] M.U. Rahim, X. Gao, H. Wu, Determination of chlorine in solid fuels using an improved Eschka method, Fuel 129 (2014) 314-317.

[12] S. Chen, K. Shehzad, X. Qiao, X. Luo, X. Liu, Y. Zhang, X. Zhang, Y. Xu, X. Fan, A high performance broadband photodetector based on (SnxSb1−x)2Se3 nanorods with enhanced electrical conductivity, Journal of Materials Chemistry C 6(41) (2018) 11078-11085.

[13] Z. Deng, M. Mansuripur, A.J. Muscat, Simple Colloidal Synthesis of Single-Crystal Sb-Se-S Nanotubes with Composition Dependent Band-Gap Energy in the Near-Infrared, Nano Letters 9(5) (2009) 2015-2020.

[14] F.A. Al-Agel, E. Al-Arfaj, A.A. Al-Ghamdi, B.D. Stein, Y. Losovyj, L.M. Bronstein, F.S. Shokr, W.E. Mahmoud, Structure and magnetic properties of diluted magnetic metal oxides based on Cu-doped CeO2 nanopowders, Ceramics International 41(1) (2015) 1115-1119.

[15] Z.M. Gibbs, A. LaLonde, G.J. Snyder, Optical band gap and the Burstein–Moss effect in iodine doped PbTe using diffuse reflectance infrared Fourier transform spectroscopy, New Journal of Physics 15(7) (2013) 075020.

[16] A. Walsh, J.L.F. Da Silva, S.-H. Wei, Origins of band-gap renormalization in degenerately doped semiconductors, Physical Review B 78(7) (2008).

[17] Y.-S. Fu, P.-Y. Lin, Mechanism of CuInSe2 nanorod formation: Cu2−xSe phase conversion induced by indium intercalated route, CrystEngComm 15(7) (2013) 1454.

[18] L.W. Khai, T.K. Hua, L. Daosheng, S. Wicaksono, Y.S. Fatt, Mid-Infrared InAs Photodetector Grown on GaAs Substrate Through Cation Exchange, IEEE Photonics Technology Letters 29(5) (2017) 458-461.

[19] T.D.C. Hobson, L.J. Phillips, O.S. Hutter, H. Shiel, J.E.N. Swallow, C.N. Savory, P.K. Nayak, S. Mariotti, B. Das, L. Bowen, L.A.H. Jones, T.J. Featherstone, M.J. Smiles, M.A. Farnworth, G. Zoppi, P.K. Thakur, T.-L. Lee, H.J. Snaith, C. Leighton, D.O. Scanlon, V.R. Dhanak, K. Durose, T.D. Veal, J.D. Major, Isotype Heterojunction Solar Cells Using n-Type Sb2Se3 Thin Films, Chemistry of Materials 32(6) (2020) 2621-2630.

[20] J.-M. Yu, J.-P. Yu, N. Wang, L.-L. Xiao, H. Wang, Q. Xu, B. Zheng, F.-F. Cheng, W.-W. Xiong, Two Series of Main-Group Heterometallic Selenides Synthesized in Two Different Types of Ionic Liquids, Inorganic Chemistry 60(7) (2021) 4337-4341.

[21] R. Huang, J. Zhang, F. Wei, L. Shi, T. Kong, G. Cheng, Ultrahigh Responsivity of Ternary Sb-Bi-Se Nanowire Photodetectors, Advanced Functional Materials 24(23) (2014) 3581-3586.

[22] K. Jang, I.-y. Lee, J. Xu, J. Choi, J. Jin, J.H. Park, H.J. Kim, G.-H. Kim, S.U. Son, Colloidal Synthesis of SnSe Nanocolumns through Tin Precursor Chemistry and Their Optoelectrical Properties, Crystal Growth & Design 12(7) (2012) 3388-3391.

[23] X. Liu, J. Chen, M. Luo, M. Leng, Z. Xia, Y. Zhou, S. Qin, D.J. Xue, L. Lv, H. Huang, D. Niu, J. Tang, Thermal evaporation and characterization of Sb2Se3 thin film for substrate Sb2Se3/CdS solar cells, ACS applied materials & interfaces 6(13) (2014) 10687-95.

[24] W. Zhao, L. Liu, M. Xu, X. Wang, T. Zhang, Y. Wang, Z. Zhang, S. Qin, Z. Liu, Single CdS Nanorod for High Responsivity UV-Visible Photodetector, Advanced Optical Materials 5(12) (2017) 1700159.

[25] G. Konstantatos, E.H. Sargent, Nanostructured materials for photon detection, Nature nanotechnology 5(6) (2010) 391-400.

[26] K. Li, C. Chen, S. Lu, C. Wang, S. Wang, Y. Lu, J. Tang, Orientation Engineering in Low-Dimensional Crystal-Structural Materials via Seed Screening, Advanced materials 31(44) (2019) e1903914.

[27] B. Pejjai, V.R. Minnam Reddy, S. Gedi, C. Park, Status review on earth-abundant and environmentally green Sn-X (X = Se, S) nanoparticle synthesis by solution methods for photovoltaic applications, International Journal of Hydrogen Energy 42(5) (2017) 2790-2831.

Caption of Figures

Figure 1 (a) XRD patterns of the bulk $Sb_2(Se_{3-x}Cl_x)_3$ crystals x=0.00,0.0008,0.0017,0.0025 and 0.0033), (b) Lattice constants a, b and c plotted as a function of Cl^- doping concentration, (c) SEM image of the $Sb_2(Se_{0.9983}Cl_{0.0017})_3$ crystal, (d) backscattered electron image of the $Sb_2(Se_{0.9983}Cl_{0.0017})_3$ crystal.

Figure 2 (a) HRTEM image of the $Sb_2(Se_{0.9983}Cl_{0.0017})_3$ crystal (the insets are the electron diffraction patterns by fast Fourier transforming of the selected area corresponding to (a), where the scale bars stand for two 1/nm), (b) XPS spectrums of different Cl^- concentration samples, (c) A plot of $[F(R)h\upsilon]^2$ vs energy for different Cl concentration samples (the inset is the corresponding optical absorption spectra), (d) electrical resistivity and carrier concentration plotted as a function of Cl^- doping concentration (x value).

Figure 3 Cl^- doped Sb_2Se_3 defect formation energy as a function of Fermi level under (a) Se-deficient and (b) Se-rich conditions. (c) Defect transition level diagram.

Figure 4 (a) schematic illustration of the 3-electrode photo-electro-chemical (PEC) measurement (b); and image of the fabricated working electrode, (c) Current-voltage characteristics of doped Sb_2Se_3 crystals as working electrodes with different Cl^- doping concentrations, (d) Current-voltage characteristics of pure Sb_2Se_3 crystal and $Sb_2(Se_{0.9983}Cl_{0.0017})_3$ crystal,(e) magnified plot of response cycle in $Sb_2(Se_{0.9983}Cl_{0.0017})_3$ and (f) response and recovery time of $Sb_2(Se_{0.9983}Cl_{0.0017})_3$.

Figure 5 (a) XRD patterns of the $Sb_2(Se_{0.99833}Cl_{0.00167})_3$ films under different annealed

temperatures. (b) Lattice constants a, b and c plotted as a function of annealed temperature, (c) texture coefficients of XRD diffraction peaks based on $Sb_2(Se_{0.9983}Cl_{0.0017})_3$ films under different annealing temperatures, (d) A plot of $[F(R)h\upsilon]^2$ vs energy.

Figure 6 Top views and cross-section SEM images of $Sb_2(Se_{0.9983}Cl_{0.0017})_3$ films on FTO substrates with different annealing temperatures: (a, b) 330 ºC, (c, d) 340 ºC, (e, f) 350 °C and (g, h) 360 ºC.

Figure 7 Photoelectrochemical response of post-annealed films on FTO with different annealing temperatures illuminated via a chopped light power density of 7 mW/cm^2 : (a) 340 °C, (b) 360 °C; Time-resolved photoresponse of post annealed films on FTO with different annealing temperatures illuminated via a light power density of 7 mW/cm^2 : (c) 340 °C, (d) 360 °C; the Magnified plot of one response cycle post annealed films on FTO with different annealing temperatures : (e) 340 °C, (f) 360 °C.

Highlights

1. The carrier concentration and electrical conductivity were raised of orders of magnitude.
2. The crystals owned a band gap around 1.10 eV, and changed from p-type to n-type.
3. The $Sb_2(Se_{0.9983}Cl_{0.0017})_3$ thin films showed preferred (hk1) texture coefficient.

Declaration of interests

☒ The authors declare that they have no known competing financial interests or personal relationships that could have appeared to influence the work reported in this paper.

☐ The authors declare the following financial interests/personal relationships which may be considered as potential competing interests: